Development of High Speed Interferometry Imaging and Analysis Techniques for Compressible Dynamic Stall

M.S. Chandrasekhara[1]
Associate Director and Research Professor
Navy-NASA Joint Institute of Aeronautics, Department of Aeronautics and Astronautics
Naval Postgraduate School, Monterey, CA 93943, U.S.A.

L.W. Carr
Research Scientist and Group Leader, Unsteady Viscous Flows,
Aeroflightdynamics Directorate, Aviation Research, Development and
Engineering Center, U.S. Army ATCOM and,
Fluid Mechanics Laboratory Branch
NASA Ames Research Center, M.S. 260-1, Moffett Field, CA 94035-1000, U.S.A.

and

M.C. Wilder
Senior Research Scientist
MCAT Inc., San Jose, CA, U.S.A.

1. SUMMARY

The development of a high-speed, phase-locked, real-time, point diffraction interferometry system for quantitative imaging unsteady separated flows is described. The system enables recording of up to 224 interferograms of the dynamic stall flow over an oscillating airfoil using a drum camera at rates of up to 40 KHz controlled by custom designed electronic interlocking circuitry. Several thousand interferograms of the flow have been obtained using this system. A comprehensive image analysis package has been developed for automatic processing of this large number of images. The software has been specifically tuned to address the special characteristics of airfoil flow interferograms. Examples of images obtained using the standard and the high-speed interferometry techniques are presented along with a demonstration of the image processing routine's ability to resolve the fine details present in these images.

LIST OF SYMBOLS

C_p	pressure coefficient
c	airfoil chord
f	frequency of oscillation, Hz
k	reduced frequency $= \frac{\pi f c}{U_\infty}$
I	image intensity
M	freestream Mach number
U_∞	freestream velocity
x,y	chordwise and vertical distance
α	angle of attack
α_0	mean angle of attack
α_1	amplitude of oscillation
ϵ	fringe number
ρ	density
ρ_0	density at atmospheric conditions
ρ_r	density at reference conditions

2. INTRODUCTION

Dynamic stall has limited the flight envelope of helicopters for many years. The problem has been studied both in the laboratory and in flight, employing complex surface measurement techniques such as pressure transducers or skin friction gauges. To properly understand the complex physics associated with dynamic stall both surface and off-surface measurements are needed simultaneously. Quantitative visualization of the flow field during compressible conditions can be used in such cases, but in the past this has been possible only through carefully aligned and meticulously reconstructed holographic interferometry.

As part of a long-range effort focused on exploring the physics of compressible dynamic stall, a research wind tunnel was developed at NASA Ames Research Center(ARC) which permits visual access to the full flow field surrounding an oscillating airfoil during compressible dynamic stall (Ref. 1). Initially, a stroboscopic schlieren technique was used for visualization of the stall process (Ref. 2), but the primary research tool has been the real-time, self-aligning technique of Point Diffraction Interferometry(PDI), which has been carefully optimized for use in this project (Ref. 2,3). PDI is a robust, self-aligning interferometry technique. It uses conventional schlieren optical components and is immune to the problems that generally limit the application of other interferometers. Using PDI, both global and surface flow features can be simultaneously documented. It has been shown in Ref. 2 that dynamic stall onset occurs over a very narrow angle of attack range ($O(0.5)$ deg), at instantaneous angles of attack when the airfoil pitch rate is maximum, during which a large leading edge vortex forms and grows rapidly from a fully attached flow. Further, hysteresis results in cycle-to-cycle variation of stall onset which smears the data if acquired by conventional ensemble averaging. Thus, it is required that the flow developments be captured in just one pitch-up cycle which places extraordinary demands on the data acquisition

[1] Mailing Address: M.S. 260-1, NASA Ames Research Center, Moffett Field, CA 94035, U.S.A.

methods. Since the pitch rate could be as large as 4000 deg/sec and the data is needed at a very high resolution to document the details of dynamic stall evolution, extremely rapid real-time imaging rates (O (20 KHz)) become necessary. It is clear that holographic techniques are not applicable here.

The recording of the rapid flow changes also requires freezing the flow events during data acquisition. This implies sampling times of less than a microsecond for the present study. The energy output of even the most powerful laboratory laser is generally less than 200 μJ for repetitively pulsed conditions. Imaging at such a low light level restricts the choice of recording systems to photographic film since even high speed videos presently do not have a satisfactory response at these low light levels. Trials showed that such systems responded randomly to individual photons of light rather than to light across the whole field of view.

One of the most valuable aspects of PDI is the fact that interferograms can be produced in real-time on a continuous basis through the use of a rapidly-pulsed laser. Pulsing at rates of up to 40 KHz and recording with high-speed film camera produces interferograms at a sufficient resolution (both in space and time) to analyse the rapidly developing unsteady dynamic stall field. In the present experiments, this has been achieved through the use of a high-speed drum camera combined with custom designed electronic circuitry. Interferogram sequences of dynamic stall development during a single oscillation cycle of the airfoil have been recorded at rates of up to 20 KHz. A detailed analysis of the effects of pitch rate, Mach number, Reynolds number, amplitude of oscillation, and other parameters on the dynamic stall process has thus become possible.

The present research has also focused on quantitative determination of the fluid physics of the compressible dynamic stall flow field, including the gradients of pressure in space and time from these interferograms. The development of image analysis techniques specific to PDI interferograms obtained here is a major effort in this quantitative evaluation. Instantaneous pressure distributions can now be obtained semi-automatically making practical the analysis of the thousands of interferograms that are produced in this research.

3. DESCRIPTION OF THE FACILITY AND MEASUREMENT TECHNIQUE

3.1. The Compressible Dynamic Stall Facility

The experimental studies were carried out in the Compressible Dynamic Stall Facility(CDSF) of the ARC Fluid Mechanics Laboratory. The CDSF is an indraft wind tunnel with a 10 in x 14 in test section and is equipped with a drive for producing a sinusoidal variation of the airfoil angle of attack. The tunnel Mach number is controlled by a choked, variable-area, downstream throat in the range of $0.1 \leq M \leq 0.5$. The flow is produced by a 6MW, 240,000 CFM continuously running evacuation compressor. The airfoil mean angle of attack can be set to $0 \leq \alpha \leq 15^0$, the amplitude of oscillation to $2^0 \leq \alpha_1 \leq 10^0$, and the oscillation frequency to $0 \leq f \leq 100 Hz$. In the CDSF a 3-inch

chord NACA 0012 airfoil is supported by pins between two 6 in diameter optical glass windows. This unique mounting method provides direct optical access to the airfoil surface permitting flow exploration using nonintrusive diagnostic techniques, Fig. 1. Tests on a 6-inch chord airfoil mounted between metal ports, with glass inserts for optical access to the first 40% chord of the airfoil are used to establish Reynolds number effects produced at a given freestream Mach number. Blockage effects due to the larger airfoil are small around dynamic stall onset angles of attack. (The correction to pressures is less than 5% at $\alpha = 10$ deg.) Encoders on the drive system record the mean and instantaneous angles of attack. The encoder signals are processed in a custom built interface known as the Oscillating Airfoil Position Interface(OAPI) which is also used for conditional sampling and phase locking.

3.2. Description of the PDI Technique

3.2.A. The Interferometry System

As stated earlier, the experimental studies used the real-time technique of point diffraction interferometry. PDI provides detailed, instantaneous and quantitative flow-field-density information, from which both surface and global pressure distributions can be derived. The PDI optical arrangement is similar to that of a schlieren system, but, as shown in Fig. 2, a laser light source is used with a beam expander to fill the entire field of view (determined by the tunnel windows) and a point diffractor (pin-hole) replaces the knife edge. The optics are aligned in the standard Z-type configuration to minimize astigmatism. Imaging optics are set up further downstream along the beam path for recording the flow.

The technique uses one single pass of the laser beam through the test section and depends upon the ability of a pin-hole created *in-situ* in a semi-transparent plate to produce the reference beam. Creation of the pin-hole requires focusing the laser beam on the plate and exposing the plate emulsion to a very high level of laser energy with no-flow in the tunnel. As the photographic emulsion burns away, a clear spot (pin-hole) appears on the plate. With the flow-on, light phase shifted by the flow density changes (signal beam) passes around this spot to produce interference fringes on a continuous basis in real-time. The portion of the beam passing through the pin-hole becomes the reference beam due to the spatial filtering characteristics of the pin-hole. The technique has now evolved considerably and several hundred interferograms can be obtained in a day's work.

3.2.B. Details of the High-Speed Camera, Laser Control and Recording Technique

A Qunatronix Series 100 CW/pumped Nd:YAG laser, capable of operating from DC to 50 KHz was used in the experiments. It could be externally triggered without any detectable delay at all rates. The pulse duration and the energy output varied nonlinearly from 85 ns and 140 μJ at 500 Hz, 420 ns and 25 μJ at 40 KHz and 100 ns and 11 μJ at 50 KHz. At the rates used for the high-speed interferometry experiments being re-

ported, the corresponding numbers were: 140 ns and 65 μJ at 10 KHz and 240 ns and 17 μJ at 20 KHz, at nearly full current settings. The energy density in the laser light pulse at the 10 KHz rate was adequate to give proper exposure on ASA 100 T-MAX film; ASA 400 film was necessary at 20 KHz.

A variable speed Cordin drum camera (DYNAFAX Model 350) was used for image recording. A rotating 8-faceted mirror in the camera reflected the incoming light beam onto film rotating in the same direction in the camera drum. Effective shutter times of 1.35 μsec could be achieved at the 40 KHz framing rate. At 20 KHz, this time was 2.7 μsec. The camera recorded two rows of 16 mm images on a 35 mm film strip, with successive exposures recorded alternately in each row, but displaced by 16 frames. A maximum of 224 frames could be recorded at any framing speed.

The laser was triggered by TTL pulses emitted by custom designed and built (in-house) circuitry installed on the camera. An infrared (IR) emitter/detector was installed in the camera (out of the light path as shown in Fig. 3) to detect reflections from the mirror facets as they passed. The selected film was not sensitive to the 940nm IR wavelength. Each mirror facet detection produced two pulses using fast rise-time (1 nsec) photo diodes to ensure adequate signal level. The pulses were delayed from the time of the IR detection pulse. The time delays were calibrated so that the mirror facet was aligned with the image frame at the time of each laser pulse. Two photo diodes were placed in the camera, one at the frame position in each film track for calibrating the time delays, then removed for operation. The tuning procedure involved adjusting two delay times with the camera running: T_1, the delay between detecting a mirror facet and emitting the first TTL pulse (the trigger pulse to the laser and for data collection) and T_2, the time between the two TTL pulses (the time between frames). The delay times T_1 and T_2 were adjusted to maximize the laser light detected by the frame photo detectors. Once tuning was properly completed, the photo detectors were moved from the field of view to permit laser light to reach the film plane. The short effective shutter times (of 1.35 μsec at the maximum camera speed) and the high framing speeds required a careful design of the electronic system that included schemes for proper attenuation of noise.

The lenses in the PDI imaging optics could be adjusted to produce a focused image of the flow area at the film plane of the camera. Aligning the camera along the optical axis of the interferometry system required very accurate adjustment.

3.2.C. Operation

The interframe pulse delay was tuned to the desired rate and the actual rate of the camera was measured using a frequency counter. Several interferogram sequences were then obtained at 11.56 KHz and 19.62 KHz for varying initial phase angles. In order to maintain a consistent pulse energy level, the laser was triggered by an external pulse train at a 40 KHz rate before the images were acquired. This was necessary to protect the laser crystal from the giant pulse that

is normally generated when the laser is pulsed after a short lapse time. In order to prevent these pulses from exposing the film and for safety reasons, a solenoid actuated laser shutter was set up in front of the laser. A hand switch was used to initiate the controlled laser pulsing sequence, which is schematically described in Fig. 4. The corresponding timing sequence is shown in Fig. 5. After the switch was pressed, the circuitry was activated by an event pulse from the OAPI corresponding to the manually preselected angle of attack which in turn triggered the laser safety shutter. The laser pulsing circuit was then inhibited (for 1.1 msec) until the laser shutter fully opened. The laser was enabled at the expiration of the delay and was actually triggered from the next camera pulse, at which time the encoder was latched and recorded in a 512 word first-in-first-out(FIFO) buffer. During this short elapsed time, the laser built up sufficient charge to cause the first pulse to be a "small" giant-pulse, which over-exposed the first frame. This frame served to identify the first image on the film strip; thus, it was possible to accurately match the interferogram images with the phase angle of motion and to correlate the values in the FIFO buffer. A frame counter, started at the first laser-pulse event inhibited the laser after 200 laser pulses. Each film strip can record a maximum of 224 images. Following the completion of the imaging, the shutter was closed and the laser returned to the constant 40 KHz external triggering. The camera alignment was verified by taking test sequences on a Polapan ASA 125 film; the data was obtained on the higher resolution T-MAX 400 film.

3.2.D. Determination of Pressure Coefficients from Fringe Number

The quantitative nature of the interferograms allowed derivation of the pressure distribution over the airfoil when the flow was attached. The interferograms were processed in a manual mode using a specially developed software package. The program read a digitized (256 gray level) interferogram on an IRIS Work Station and over-layed an airfoil using the registration markers on the images. The intersection of the fringes with the airfoil upper and lower surfaces (or the local boundary layer edge, when detectable) were interactively picked by the user. Since each fringe is a line of constant density, the corresponding pressure at the boundary layer edge could be calculated using isentropic flow relations. This pressure was then used as the surface pressure, under the boundary layer assumptions. The density along any fringe could be calculated from the Gladstone - Dale equation, which for the present wind tunnel and laser simplifies to

$$\rho - \rho_r = 0.009421\epsilon$$

where ϵ, the fringe number, is $0, \pm 1, \pm 2,...$ for the bright fringes and $\pm\frac{1}{2}, \pm\frac{3}{2}, \pm\frac{5}{2},...$ for the dark fringes. Fringes from the free stream to the stagnation point have positive values. The corresponding C_p values were then computed from the relation

$$C_p = \frac{\left[\left(\frac{\rho}{\rho_r}\right)^\gamma - 1\right]}{\left[\frac{\gamma}{2}M^2\right]}$$

In the end, the program provided an output data file containing the various physical variables, in a format suitable for plotting. Typical processing time was about 3 - 5 minutes per image. In cases where the fringe density was high or the fringes were fuzzy, the user could go into the 'off-body' mode and pick fringes along a line parallel to and away from the airfoil surface where the fringes are farther apart. For this purpose, an option to superpose two larger airfoils over the image on the screen was provided. The fringe intersections on the larger airfoils were then suitably projected on to the airfoil surface. At angles of attack near the dynamic stall angle, the fringes near the leading edge region were very dense reflecting the large local density gradients. Further, in this region, optical noise introduced by the shadowgraph effect generally lowered the contrast, making it a location where the off-body mode needed to be invoked.

In the present study the entropy change in the vortical flow was ignored (for lack of a better method). Interferograms with shocks have not been processed for pressures because of this limitation.

3.3. Details of Image Processing

Aside from these manual procedures, a program was also developed for automatic analysis of the interferograms. A number of digital filters and image enhancement procedures are available. The operator is required to register the image (thus masking the airfoil and establishing a coordinate system), choose the filtering and/or enhancement methods, and mark regions of the image for special treatment. Fringe centerlines are automatically traced with processing times approximately one quarter that of fully-manual processing, and operator bias (a potential source of error in the tracing of fringes) is eliminated.

Full automation of image processing requires software capable of addressing the special characteristics of these images, such as variations in lighting and contrast across an image that are inherent to the technique, an occasional broken (or split) fringe, the high fringe density near the suction peak (as many as 50 fringes/mm along the airfoil surface), presence of shocks, etc. Full details of the image processing method, e.g. image filtering, fringe centerline detection, fringe identification, etc., can be found in Ref. 5. The flow chart shown in Fig. 6 illustrates the typical processing procedure. The need for the spin filter, an intensity gradient aligned spatial filter (Ref. 7), depends on the quality of the original image. Filtering and/or contrast enhancement are performed primarily to improve edge detection, the first stage in fringe centerline detection, as described below. For the results presented here, the region around the leading edge of the airfoil was magnified and treated separately from the rest of the image.

Fringe centerlines are located by identifying the local extrema in the image intensity. These extrema are identified within the background noise through a two-stage procedure which first locates the fringe edges, and then fits a smooth polynomial to the data between successive edges. The location of the extreme value of the approximated data is taken as the location of the fringe centerline. This procedure is a one dimensional operation performed in two passes over the image; rows of pixels are examined in the first pass and columns are examined in the second pass.

A zero-crossing algorithm is used to identify the fringe edges. The zero-crossing threshold level is either the mean intensity along the row or column of pixels under consideration, or the global mean intensity of the image. The global mean is used if the current row or column follows a fringe or crosses only one edge. A noise band around the threshold is specified to eliminate hysteresis crossings due to noise in the image.

The edges are used as a guide to locating the fringe centerlines. Assuming that each successive pair of edge points outline a single fringe, the centerline of the fringe will pass through the point of extreme intensity between these two edge points. In order to unambiguously locate this extreme, a smooth polynomial curve is fit to the data between pairs of edge points using Chebyshev approximation. The image intensity is approximated on the interval [-1, 1] as

$$I(x) \approx \sum_{k=0}^{m-1} c_k T_k(x) - \frac{1}{2}c_0$$

where the Chebyshev polynomials and the coefficients are given by

$$T_k(x) = \cos(k \cos^{-1}x)$$

and

$$c_k = \frac{2}{N} \sum_{j=1}^{N} I(x_j)T_k(x_j)$$

respectively, and the data ($I(x)$) and the Chebyshev polynomials ($T_k(x)$) are evaluated at the N zeros of $T_N(x)$, namely

$$x_j = \cos\left(\frac{\pi(j - \frac{1}{2})}{N}\right) \qquad j = 1, 2, ..., N.$$

The coefficients are calculated for Chebyshev polynomials of degree N, while the approximating polynomial is truncated to a polynomial of degree $m \ll N$ (typically $N = 20$, $m = 3$). This yields an accurate approximation of degree m to the data [8]. For sufficiently large N, as $m \to N$ the approximating polynomial reproduces the original data, including the noise. Due to the multiple inflection points in the data, approximating data spanning more than one fringe requires a higher order polynomial (m), which tends to reproduce the noise content. Therefore, the approximation procedure is confined to a single fringe.

This procedure was tested on simulated fringe data (a modulated cosine function with added Gaussian noise) and was found to be accurate to within 2 pixels for

fringes from 5 to 40 pixels in width and to within 5 pixels for fringes up to 240 pixels wide.

The points located this way comprise two sets of pixels, one associated with the dark fringe centerlines and the other with the light fringe centerlines. These data sets form two search lists which are sorted into smaller groups, each tracing a single fringe. Tracing begins arbitrarily with the first point in the search list. A nearest neighbor search is performed with an inner and outer search radius. Any point within the inner search radius of the current point is automatically designated as belonging to the current fringe. Any point found between the inner and outer search radii are assigned to the current fringe if certain criteria are satisfied. These criteria are designed to prevent the tracing procedure from bridging adjacent fringes by examining the image intensity across the gap and by checking for the presence in the gap of data points belonging to the opposite fringe type. Each data point assigned to a fringe is removed from the search list. The search is then repeated relative to each new point added to the fringe in the previous search. The search ends when the end of the fringe is reached or when a gap larger than the outer search radius is encountered. A new fringe is designated and the tracing procedure begins anew with the first point in the search list becoming the first point in the new fringe. The tracing is progressively faster as data points are removed from the search list and placed in fringe lists.

The inner search radius is two pixels, hence, any one-pixel gaps in the data are automatically bridged. The outer radius varies with fringe spacing and is six pixels in the outer flow regions where the fringe spacing is wide, and reduces to three pixels near the leading edge where fringe spacing is often less than five pixels. Due to the small fringe spacing in this region any noise in the data can cause the fringe tracing algorithm to erroneously join fringes together. Therefore, the leading edge is generally treated separately in the form of a magnified image segment.

3.4. Experimental Uncertainties

The uncertainty in C_p depends on the fringe number under consideration and is 1 fringe for the flow in general with about 3 fringes possibly undetectable near the suction peak at M = 0.3. Since correction for solid and wake blockage was less than 5% for $C_p = -6.0$ at M = 0.3, only uncorrected PDI derived pressures are reported. The losses in the tunnel screens causing a decrease in the stagnation pressure have been included in the computation of the reference density in this otherwise atmospheric flow wind tunnel.

By far the largest uncertainty appears from the very strong density gradients near the airfoil leading edge which introduces strong refractive index gradients. The effect of this is to deflect the light rays towards higher density regions. Hence, a dark region develops on the upper surface near the leading edge (Ref. 6) in some images. No corrections were applied to the C_p values on this account because of the strong dependence of the local density on instantaneous angle of attack, freestream Mach number, and reduced frequency. Also, it was found that by slightly realigning

the PDI optics, much of the distortion could be reduced. With this solution, it was estimated that the true suction peak location could be displaced by less than 0.5% of airfoil chord towards the trailing edge. Support for this can be found by directly comparing the pressures measured using surface taps and those obtained with PDI as shown in Fig. 7 (Ref. 9) for the 6-inch airfoil in steady flow at M = 0.3. At $\alpha = 8$ deg, Fig. 7a, the two agree very well. At $\alpha = 13$ deg, Fig. 7b, there is agreement to within the one fringe standard uncertainty of the PDI method. The differences seen at the laminar separation bubble location are due to the insufficient number pressure taps over the airfoil that make it impossible to record the pressures at the resolution of PDI.

With these considerations in mind, the following are the estimated uncertainties in the data:

Mach number:	± 0.005
angle of attack:	0.05 degrees
reduced frequency:	0.005
C_p:	± 0.1 at M = 0.3
$C_{p_{min}}$:	-0.5 at M = 0.3
	-0.45 at M = 0.4

4. RESULTS AND DISCUSSION

Figure 8 presents two interferograms obtained in the studies at M = 0.3, k = 0.05 and $\alpha = 10$ deg. Fig. 8a shows a standard PDI interferogram, whereas that in Fig. 8b was obtained using the high-speed PDI imaging method at a filming rate of 11.56 Khz. The sharpness of the image in Fig. 8a indicates the quality of the pictures that can be obtained with PDI. The high-speed image in Fig. 8b is still clean even after a linear magnification of about 35. The figure shows a stagnation point on the lower surface and as the flow accelerates, a laminar separation bubble forms downstream of the suction peak. The separation bubble can be inferred where the fringes running parallel to the upper surface abruptly turn normal to the surface. The parallel fringes represent the plateau in the pressure distributions due to the presence of the bubble. In both figures, a slight dark bulge is noticeable near the airfoil leading edge, which is attributed to the steep local density gradient. The global pressure maps are shown in Fig. 9 for the airfoil at an instantaneous angle of attack of 13.99 deg. The comparison also clearly illustrates the differences that can be present in the flow from one oscillation cycle to the next at angles near the dynamic stall onset angle. These differences are especially critical when considering dynamic stall control. Our work has shown that dynamic stall for these test conditions arises from the bursting of a laminar separation bubble, which occurs when the instantaneous pressure gradient exceeds a critical value and so the envelope of activation of a control devise for manipulating the adverse pressure gradient will change for each cycle.

Figure 10 shows the effects of pin-hole size on the PDI images at M = 0.4. Evaluation of the pin-hole requires recording PDI images on polaroid film. The photographic plate needs to be pre-developed to a level of darkness that results in an optical density of around 1.0. The PDI images were found to be generally insen-

sitive to the shape and size of the PDI spot in the range tested as long as the spot is smaller than the Airy disk diameter of the laser beam. Good interferograms were obtained with pin-holes created by images of both the nearly circular windows and the L-shaped optical glass inserts. The most noticeable effect of a large pin-hole is the many split fringes that form as seen in Fig. 10. These can lead to an incorrect counting of the fringes, causing erroneous pressure distributions to be derived from the automated processes. It should be noted that satisfactory interferograms have been obtained in these studies over a range of pin-hole sizes. Also, somewhat large pin-holes are needed as the flow Mach number increases due to the large density gradient and hence a larger deflection of the laser light near the leading edge. Images can be obtained reliably without much effort if a PDI plate with the right optical density is used for each Mach number. In general, it has been found that a dark plate (optical density of the $O(1)$) is needed to properly capture the finer flow details for the Mach numbers in the range of 0.3-0.45. Lighter plates worked well at lower Mach numbers.

Figures 11 and 12 show the results that have been obtained with the automated image processing program for M = 0.3 and M = 0.45 respectively. The image in Fig. 11a shows the airfoil at α = 8.84 deg for M = 0.3 and k = 0.05. The corresponding map of the dark fringes is plotted in Fig. 11b. Fig. 12a and 12b show, respectively, an image and its fringe map obtained at M = 0.45, k = 0.05 and α = 10° on the upstroke. Under these conditions the local velocity exceeded the sonic speed and an oblique shock formed. Moreover, the interaction between the shock and the laminar boundary ayer (Re = 9×10^5) resulted in the formation of multiple shocks. An enlarged view of the leading edge is shown to emphasize the shocks. The image was magnified by three and was contrast enhanced. No filtering was required. Despite the tight fringe spacing, and distortions due to the shocks considerable success has been achieved in processing the image without manual intervention. Typical processing times were about 5 min. with complicated images requiring longer times.

5. CONCLUSIONS

A novel high-speed, real-time, phase-locked, interferometry system has been developed and applied to study oscillating airfoil compressible dynamic stall flow fields. The technique can generate very sharp images of the flow over an airfoil and can capture the rapid evolution of shocks in this complicated flow. A maximum of 224 interferograms per test condition at rates of up to 40 KHz can be recorded using the system. To date, several thousand images have been obtained at rates of up to 20 KHz. A comprehensive image processing software package has also been developed for processing these large number of interferograms. The software has reduced the time required for this task considerably. It includes features for special treatment of each image using digital filtering, contrast enhancement, local magnification for high fringe density regions, accurate fringe centerline detection, fringe identification, etc. Interferograms containing multiple shocks in the flow have also been satisfactorily analyzed. The effects of vari-

ables such as PDI plate optical density, pin-hole size, etc., have been investigated The technique is robust, easy to set-up and offers considerable advantages over other interferometric methods. It is a real-time, self-aligning technique and is not affected by extraneous influences such as tunnel vibrations.

Acknowledgements

References

1. Carr, L.W. and Chandrasekhara, M.S., "Design and Development of a Compressible Dynamic Stall Facility", J. Aircraft, *29*, 3, pp. 314-318, 1992.

2. Chandrasekhara, M.S. and Carr, L.W., "Compressibility Effects on Dynamic Stall of Oscillating Airfoils", in "Aerodynamics and Aeroacoustics of Rotorcraft", AGARD-CP-552, Aug. 1995, Paper 3.

3. Brock, N.J. Chandrasekhara, M.S. and Carr, L.W., "A Real Time Interferometry System for Unsteady Flow Measurements", *ICIASF '91 RECORD*, IEEE Publication 91CH3028-8, pp. 423-430.

4. Chandrasekhara, M. S. Squires, D.D. Wilder, M.C. and Carr, L.W., "A Phase-Locked High-Speed Real-Time Interferometry System for Large Amplitude Unsteady Flows", Expts. Fluids, *20*, 1995, pp. 61-67.

5. Wilder, M.C. Chandrasekhara, M.S. and Carr, L.W., "Computer-Aided Analysis of Interferometric Images of Unsteady Aerodynamic Flows", *ICIASF'95 RECORD*, IEEE Publication 95-CH3482-7, pp. 44.1-44.11.

6. Cho, Y.C. Carr, L.W. and Chandrasekhara, M.S., "Corrections to Fringe Distortion due to Flow Density Gradients in Optical Interferometry", AIAA 93-0631, January 1993.

7. Yu, Q., "Spin Filtering Processes and Automatic Extraction of Fringe Centerlines in Digital Interferometric Patterns", Applied Optics, *27*, 18, September 1988, pp. 3782-3784.

8. Press, H.P., Teulolsky, S.A., Vetterling, W.T., and Flannery, B.P., "Numerical Recipes in C", Cambridge, U.K., Cambridge University Press, 1992, (ISBN 0-521-43108-5), pp. 190-196.

9. Chandrasekhara, M.S. Wilder, M.C. and Carr, L.W., "Reynolds Number Influence on 2-D Compressible Dynamic Stall", AIAA 96-0073, January 1996.
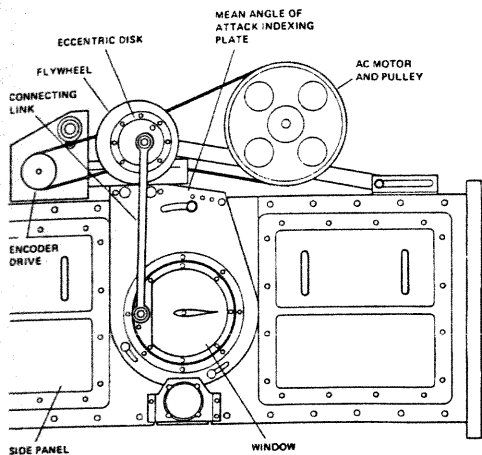
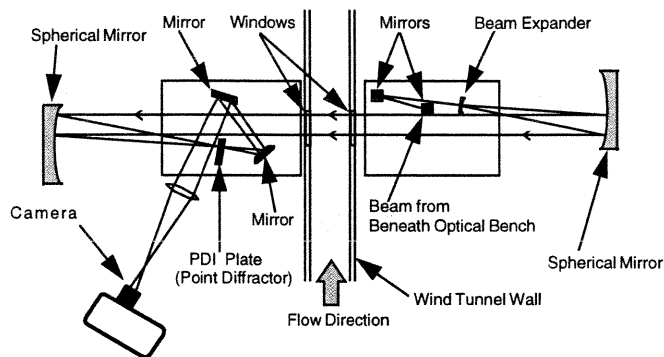Fig. 1. Schematic of the Compressible Dynamic Stall Facility.

Fig. 2. Schematic of the Point Diffraction Interferometry System.
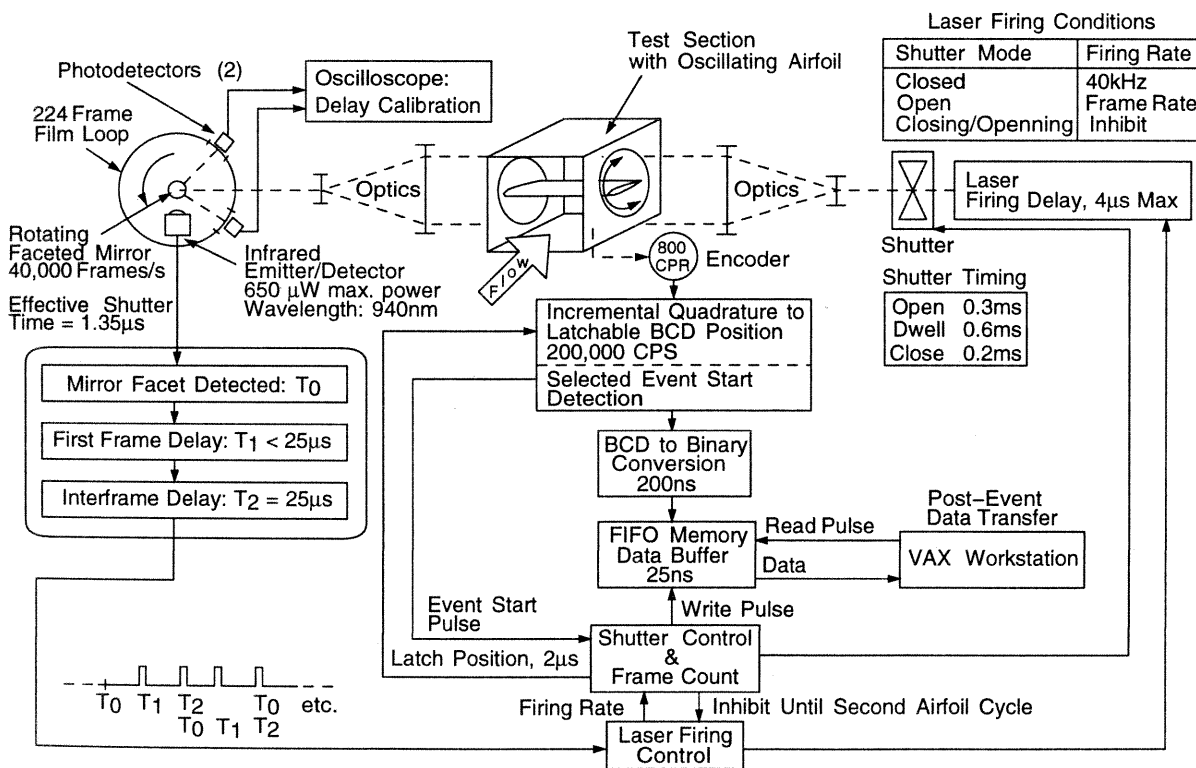

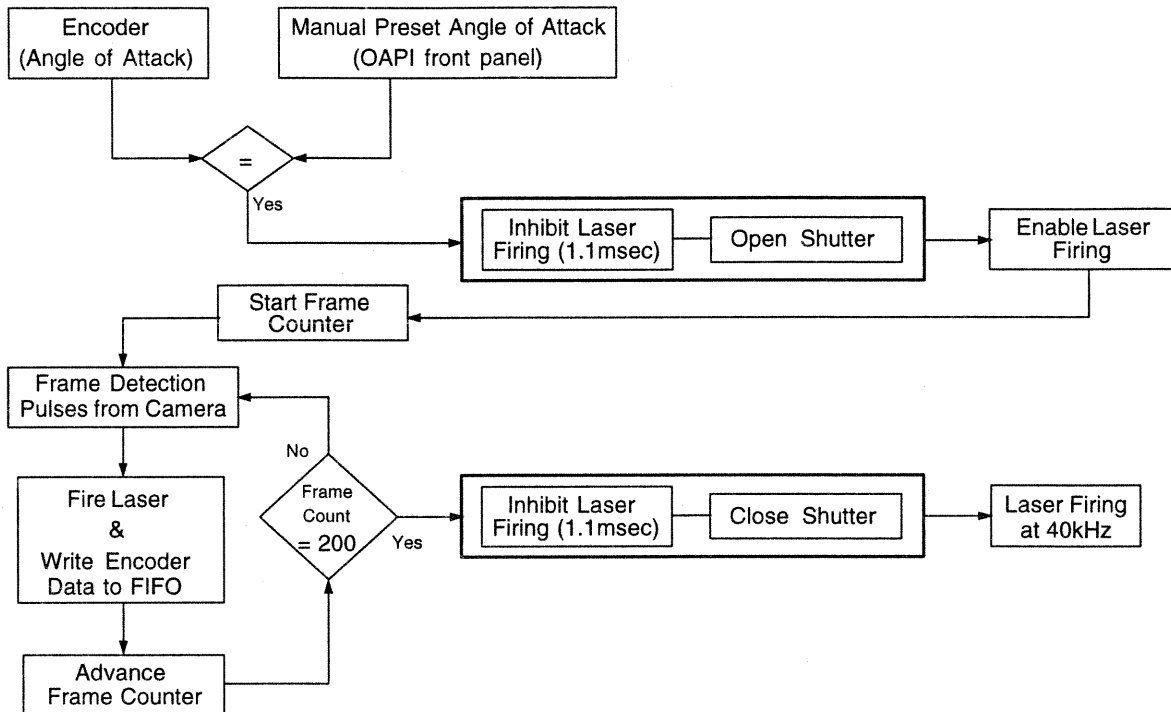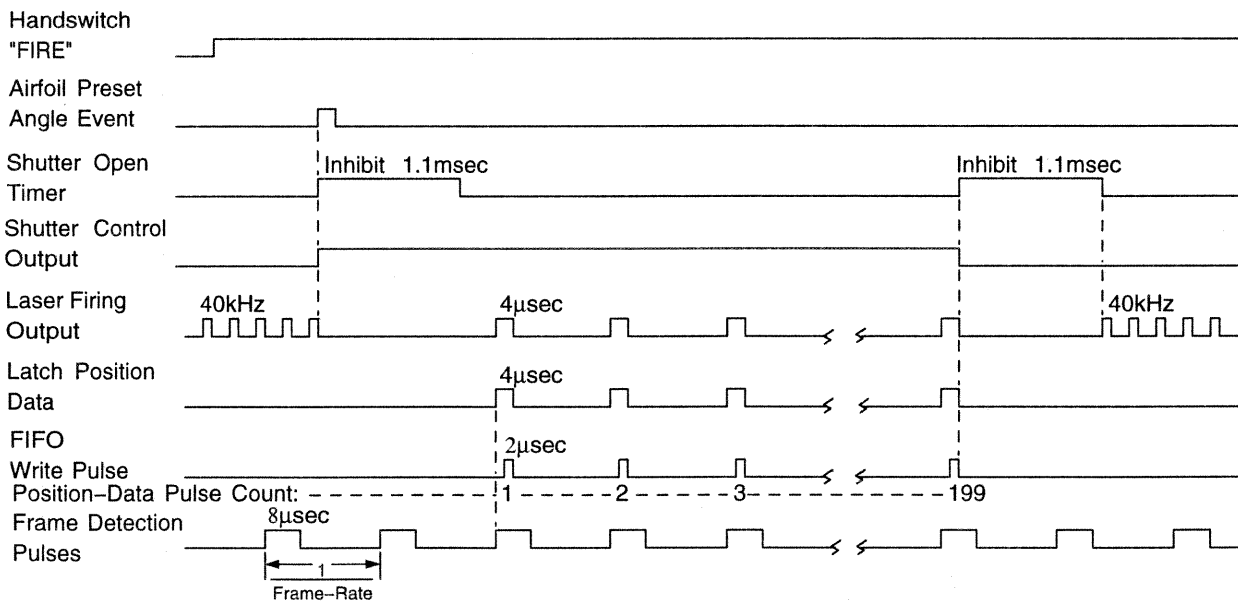Fig. 3. Block Diagram of Camera/Laser Synchronization for the High-Speed PDI System.

Fig. 4. Flowchart of Events Following Handswitch "FIRE" for the High-Speed Interferometry System.

Note: Event edges are shown in proper sequence, but not properly scaled. Refer to the pulse durations shown.
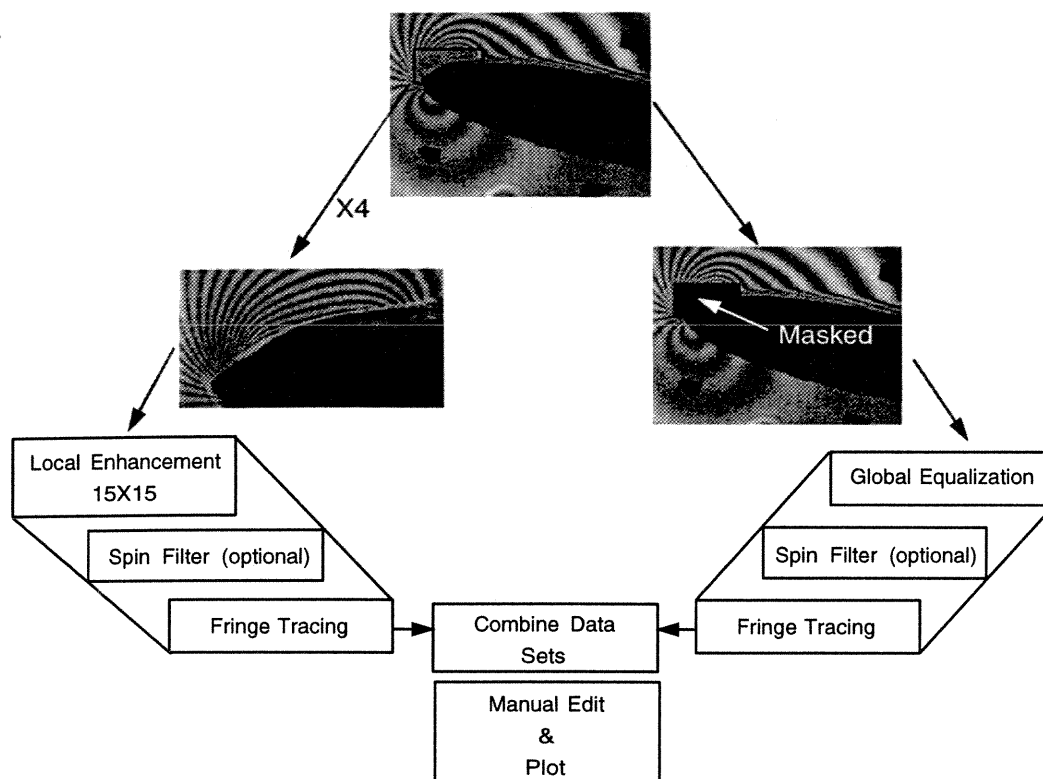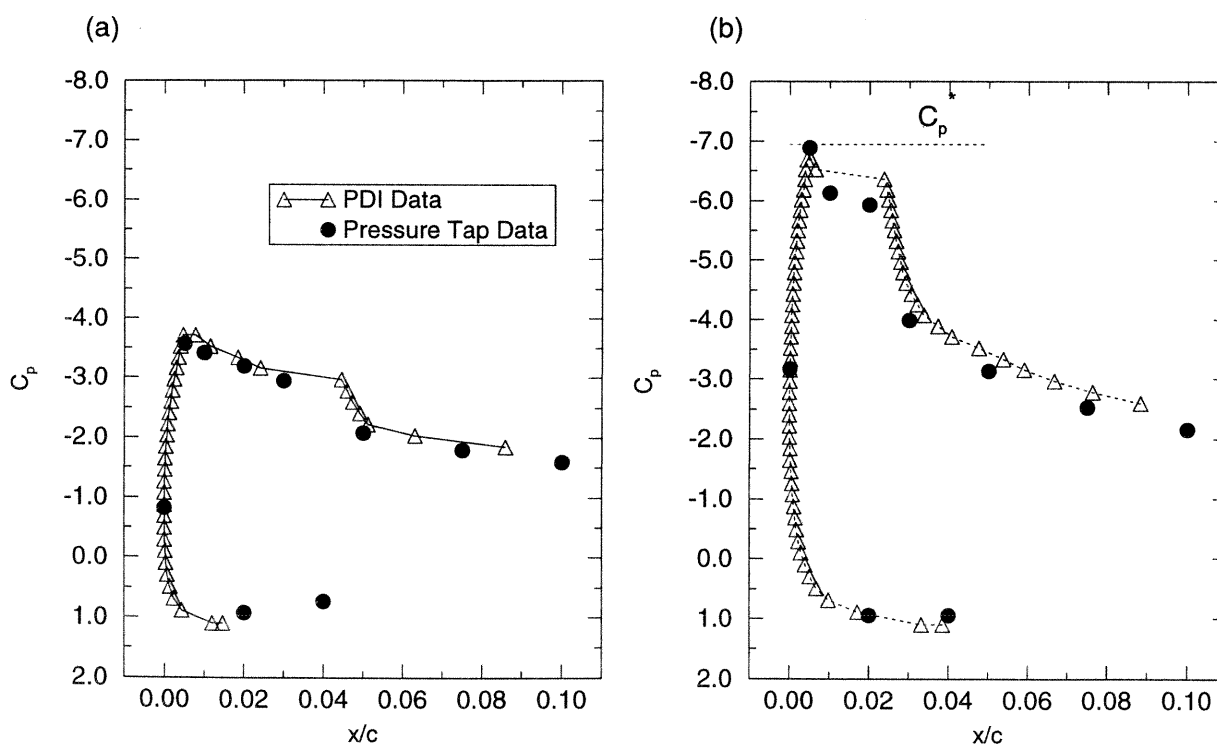
Fig. 5. Timing Sequence for the High-Speed Interferometry System.

Fig. 6. Flow Chart of Fringe Analysis Procedure.

Fig. 7. Comparison of Pressure Tap Measurements with PDI Determined Pressure Coefficients; M = 0.3, k = 0. (a) α = 8.0 deg, (b) α = 13.0 deg.

(a)

(b)
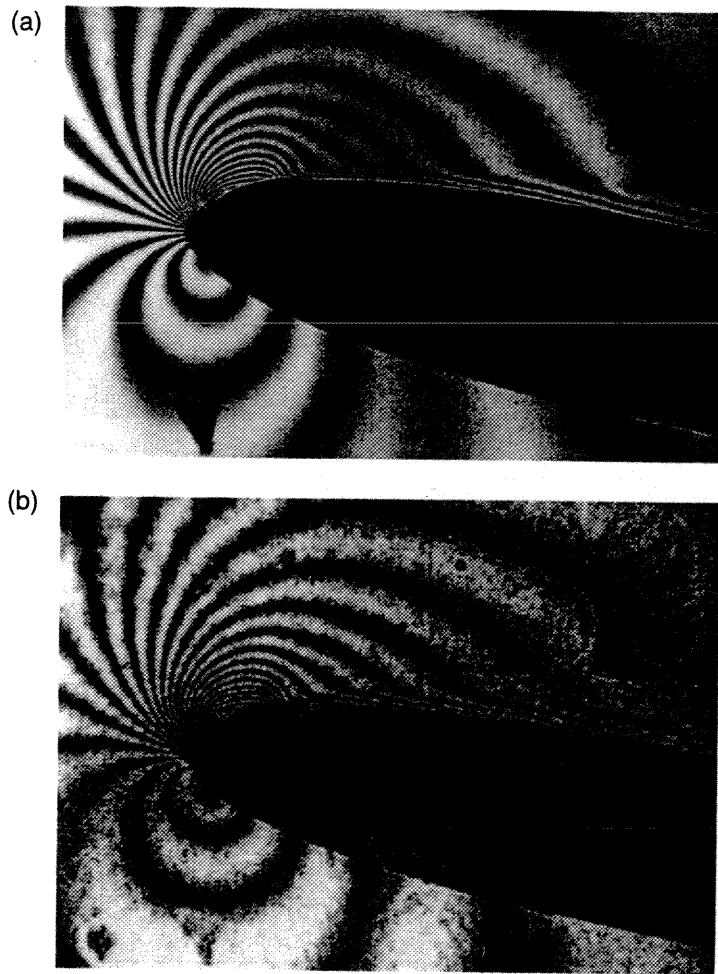
Fig. 8. Representative Interferograms of the Flow Field; M = 0.3, k = 0.05, α = 10.07 deg. (a) Single Exposure Camera, (b) High-Speed Camera.

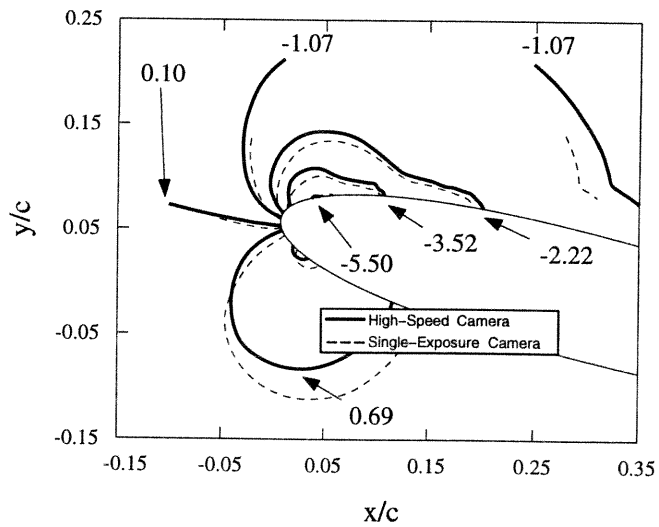Fig. 9. Comparison of the Global Pressure Distributions at M = 0.3, k = 0.05, α = 13.99 deg for Different Oscillation Cycles.

(a)

(b)
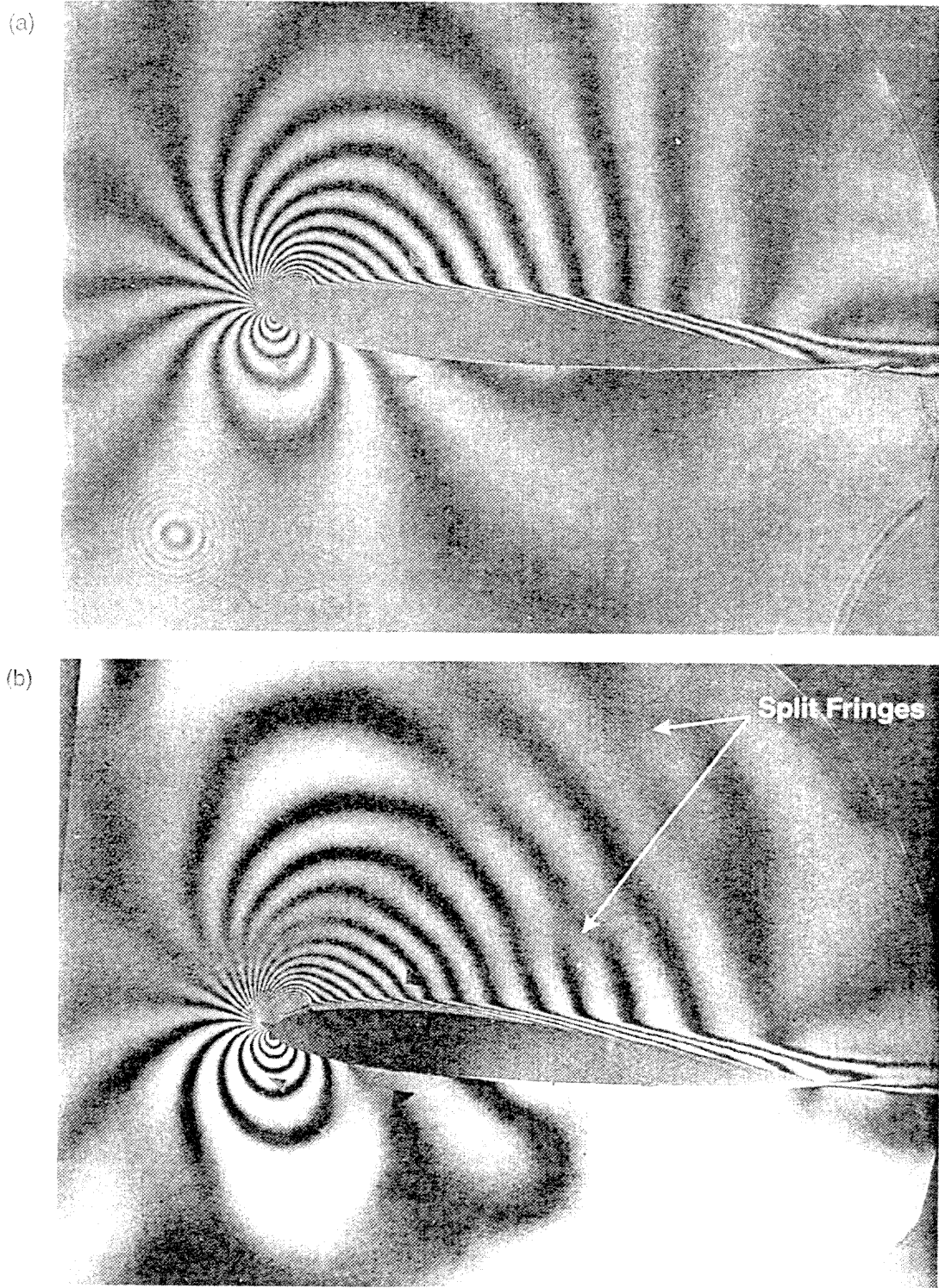
Split Fringes

Fig. 10. Effect of Pin-Hole Size on PDI Images; M = 0.4, k = 0, a = 8 deg.
(a) Small Pin-Hole, (b) Large Pin-Hole.

(a)

(b)

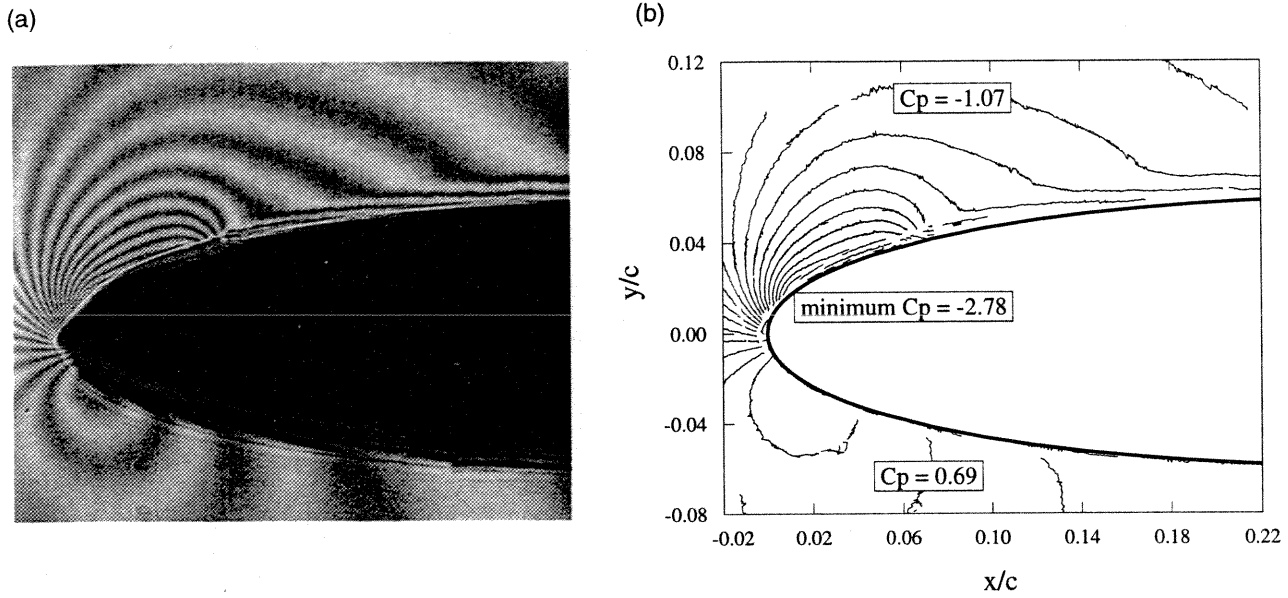

Fig. 11. Automated Image Processing; M = 0.3, k = 0.05, α = 8.84 deg. (a) Leading-Edge Region of PDI Image, (b) Map of Dark Fringes.
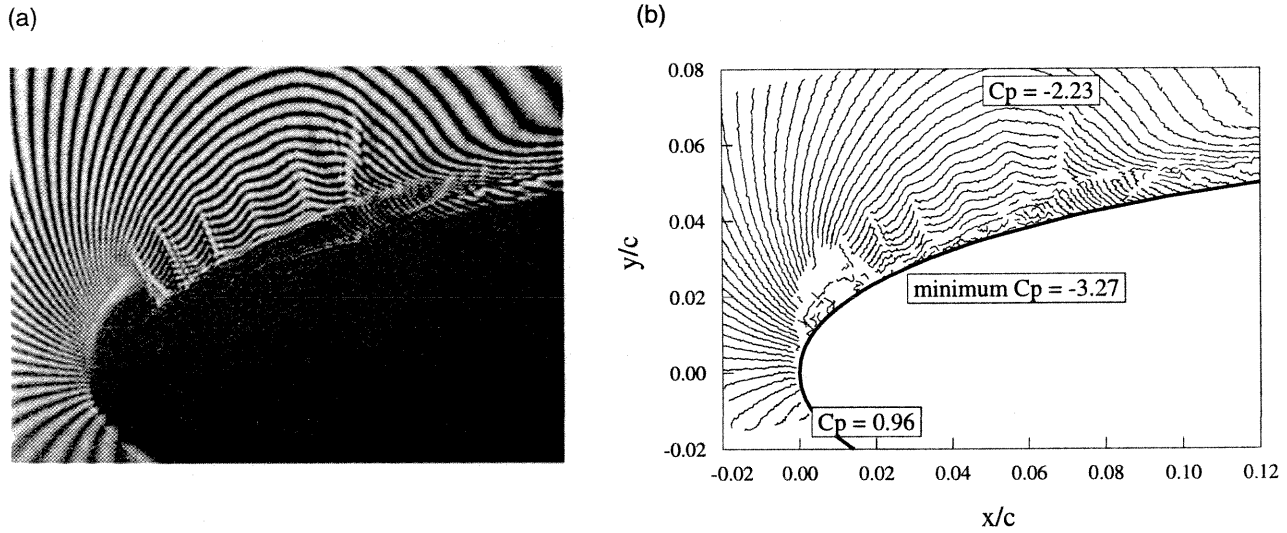
(a)

(b)

Fig. 12. Automated Image Processing; M = 0.45, k = 0.05, α = 10.0 deg. (a) Digitally Enlarged Region of PDI Image, (b) Map of Dark Fringes.